CHEMISTRY OF MATERIALS

pubs.acs.org/cm

Article

Pivotal Role of A-Site Cations in Tailoring the Band-Edge States, Optical Properties, and Stability of 0D Hybrid Indium Chlorides

Anuraj S. Kshirsagar, Yashpal Singh, Udara M. Kuruppu, Bruno Donnadieu, Neeraj Rai,* and Mahesh K. Gangishetty*

Cite This: *Chem. Mater.* 2022, 34, 10928−10939

Read Online

ACCESS | Metrics & More | Article Recommendations | Supporting Information

ABSTRACT: Optoelectronic properties of organic−inorganic hybrid perovskites (ABX_3) or metal halides are governed primarily by the B and X-site ions due to their electronic contribution to the band edge. The A-site cations do not directly participate in the band edge; instead, they stabilize the crystal structures. Facilitating these A-site cations to contribute to the band edge can enable an additional degree of tunability to properties and expand the opportunities beyond B and X ions. Here, we rationally employ different A-site cations based on anilinium cations in Sb^{3+}-doped zero-dimensional (0D) indium chlorides and illustrate their contribution to the band-edge states using experimental data and theoretical calculations. We demonstrate that a change in the A-site cation results in a change in the octahedral distance in the crystal structure. In addition to this, we show that the frontier orbitals of hybrid indium chlorides are delocalized across the inorganic and organic moieties, leading to significant changes in their optical properties. Consequently, Sb^{3+}-doped hybrid indium chlorides show a broadband emission with a PLQY over 93% and remarkable spectral and structural stability in five different solvents, including water, for 21 days.

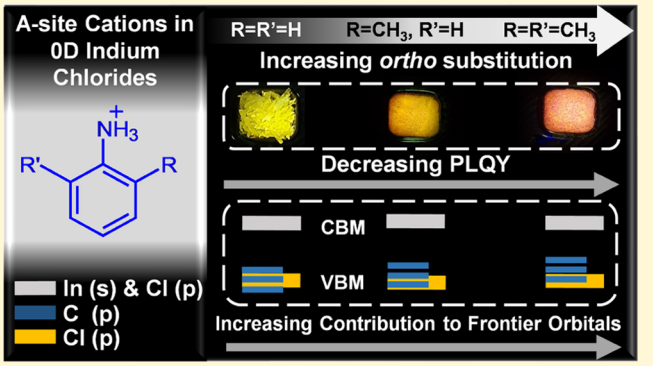

INTRODUCTION

Compositional tuning in metal halide perovskites (ABX_3, where A is a monovalent cation, B is a divalent cation, and X is a halide anion) and hybrid metal halides is a widely known strategy to achieve exciting optoelectronic properties. Due to the flexible nature of the lattice, it can sustain the manipulation of A, B, and X composition.[1−5] In perovskite lattice, inorganic B and X ions form octahedral $[BX]_6^{2-}$ centers, and these centers are primarily responsible for both optical and electronic properties of perovskites. For example, the band-edge structure in $CsPbX_3$ (valance band maximum (VBM) and conduction band minimum (CBM)) is composed of 6s and 6p orbitals of Pb^{2+} and 3p-orbitals of halides.[4,6] Therefore, most optical and electronic transitions are localized on B and X sites. As a result, many reports focus on changing B and X-site ions to tune the emission and electronic properties of perovskites. The seminal work by Kovalenko and co-workers shows the color tunability across the wavelengths in $CsPbX_3$ (X = Cl, Br, and I) by simply changing the halide ion.[7] Substitution of B-site Pb^{2+} with homo- and hetero-valent cations has led to a new class of perovskites, including double perovskites, and hybrid metal halides with reduced dimensionality and significantly different optical and electronic properties.[8−15] Although most hybrid metal halides do not follow perovskite (corner-sharing octahedra) crystal structure, they show exciting optical properties similar to perovskites. To tune the optoelectronic properties of metal halides, generally, the efforts are more focused on changing B and X sites like in perovskites. Therefore, the choice of both B and X sites provides an opportunity to obtain desired properties for optoelectronic applications.[16−20]

In contrast, it is believed that the A-site cations do not directly contribute to the band edge; instead, their electronic states are buried deeper into the VB and CB away from the band edge. Therefore, tuning optoelectronic properties by varying A-site cations has always been limited.[21,22] However, these A-site cations play a critical role in phase stabilization, hydrophobicity/water stability, suppression of ion migration, surface functionalization, surface energy manipulation, and change in electronic dimensionality of hybrid metal halides.[22] Typical A-site cations consist of protonated organic amines such as methylammonium (MA), ethylammonium (EA), formamidinium (FA), phenethylammonium (PEA), methyl-

Received: September 16, 2022
Revised: November 27, 2022
Published: December 14, 2022

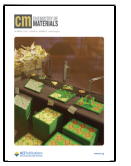

https://doi.org/10.1021/acs.chemmater.2c02737
Chem. Mater. 2022, 34, 10928−10939

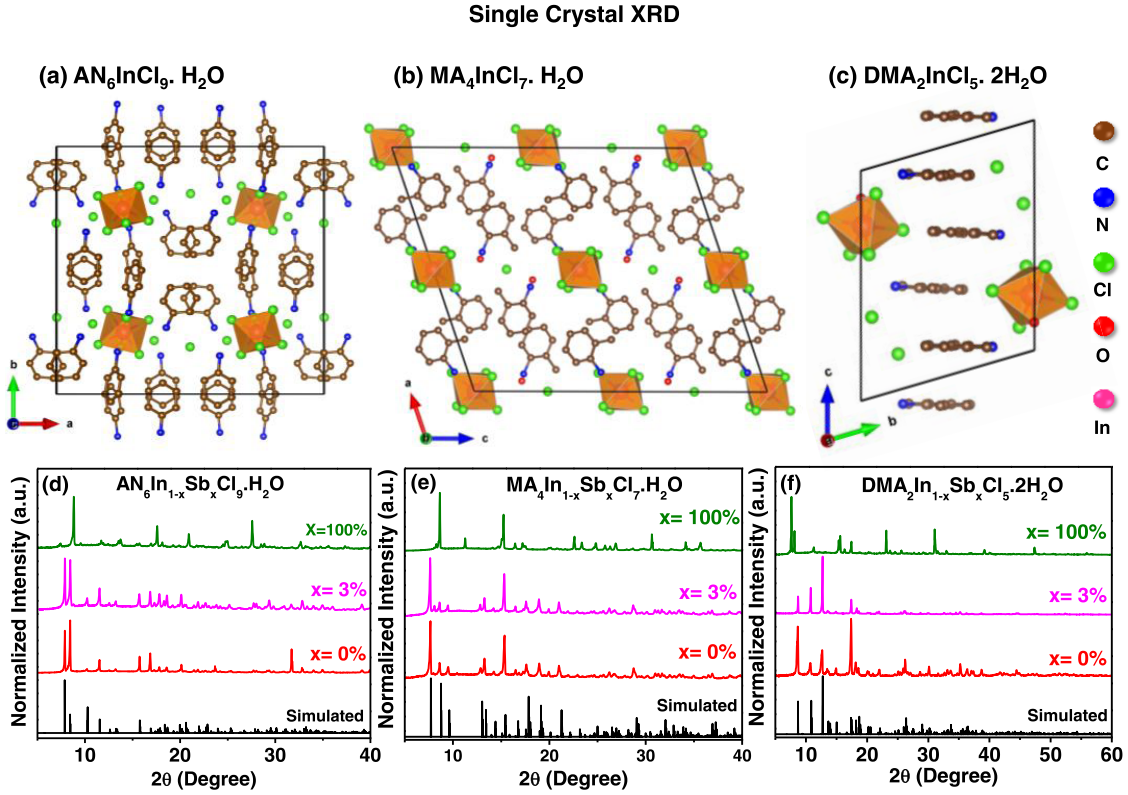

Figure 1. Crystallographic analysis of 0D hybrid indium chlorides. Crystal structures of (a) $AN_6InCl_9{\cdot}H_2O$ (AIC), (b) $MA_4InCl_7{\cdot}H_2O$ (MIC), and (c) $DMA_2InCl_5{\cdot}2H_2O$ (DIC) obtained by single-crystal XRD data refinement. Hydrogen atoms are omitted for clarity. (d–f) Powder XRD patterns of undoped and Sb^{3+}-doped AIC, MIC, and DIC. The green-colored patterns are for the compounds prepared without the indium precursor (100% Sb).

enediammonium (MDA), dimethylammonium (DMA), or alkali metal cations (Na^+, Cs^+, Rb^+).[23−26] Organic A-site cations with ionic radii comparable to Cs^+ (e.g., MA, and FA) form a three-dimensional (3D) perovskite structure, often with cubic symmetry ($Pm3m$ space group).[21] The dimensionality of the perovskite is often regulated by the size of A-site cations.[22] Large organic spacers such as PEA, piperidinium, butyl ammonium, and pyrene can result in two-dimensional (2D), one-dimensional (1D), and 0D hybrid metal halides with or without retaining the perovskite crystal structure.[27−30] Such hybrid metal halides have been finding their unique applications in light-emitting diodes (LEDs), photovoltaics, thermography, photodetectors, X-ray scintillators, and anti-counterfeiting.[31−36] Recently, 0D metal halides such as $MA_4PbX_6{\cdot}2H_2O$, $A_3Cu_2I_5$, and Sb^{3+}-doped $A_2InX_5{\cdot}H_2O$ (A = Cs, Rb, X = Cl, Br) have attracted perovskite field owing to their exceptional PLQYs over 90%, strong exciton-binding energy, broad emission spectra potential for white emission, and great thermal, and environmental stability.[37−40] Although the 0D metal halides have been known for a century, their optoelectronic properties are now increasingly explored for device applications.[41]

Several recent reports on 0D hybrid metal halides have observed room temperature phosphorescence using selective organic A-site cations and inorganic B and X ions. For example, Wei et al.[33] demonstrated the afterglow green and white emission using BAPP (1,4-bis(3-aminopropyl)piperazine) as A-site cations in Sb/In halide perovskites. Ma and co-workers showed efficient long-living phosphorescence emission using tetraphenylphosphonium (TPP) in selective 0D metal halides.[42] Lin and co-workers recently observed blue phosphorescence from aniline hydrochloride as an A-site cation in 0D In-chlorides. They demonstrated that the delayed blue emission is due to the interactions of molecular triplet states with the heavy metal atom at the B site.[34] However, the precise mechanism of this energy transfer is not known and needs a detailed spectroscopic investigation. While it is encouraging that selective A-site cations can facilitate energy transfer, carrier dynamics, such as carrier injection and transport, which are crucial for device applications, are primarily influenced by the band-edge contribution of A-site ions.[30] Notably,[43,44] in the case of 0D metal halides, the poor charge transport owing to isolated inorganic centers is one of the critical challenges, thus limiting them from excelling in the LED field despite their exceptional PLQYs. One promising approach to overcome this challenge is employing conjugated organic cations, which can contribute to the band-edge states and facilitate the delocalization of excitons with frontier orbitals spanning across organic and inorganic moieties.[30,44,45] So far, only one study by Yang and co-workers demonstrated the contribution of A-site cations to the band-edge states in 2D perovskites. Using conjugated pyrene-based amines such as pyrene ethylammonium (PREA) at the A-site in 2D perovskites, they observed a change in the position of VBM. Further, by incorporating these 2D perovskites in solar cells, the overall power conversion efficiency of perovskites is improved.[30] A recent perspective on "Rethinking of A cation" by Park and co-workers highlights the scope of A-site cations beyond their traditional role in stabilizing the structure. Therefore, the contribution of the A-site can be improved in the band-edge

https://doi.org/10.1021/acs.chemmater.2c02737
Chem. Mater. 2022, 34, 10928−10939

state by engineering the interactions between organic and inorganic parts of hybrid metal halides.

Here, we demonstrate the critical role of conjugated anilinium A-site cations in (1) altering the band-edge states, (2) achieving high photoluminescence (PL) quantum yields with broad color tunability, and (3) stabilizing the crystal structure in various solvents, including water, with a remarkable emission recovery. We employed three A-site cations, anilinium (AN), 2-methyl anilinium (MA), and 2,6-dimethyl anilinium (DMA) to form 0D Sb^{3+}-doped (and undoped) indium chlorides. These A-site cations contain the amine groups directly attached to the benzene rings, unlike several aromatic organic amines where the methyl/ethyl (aliphatic) groups separate the amine group from benzene rings. The direct bond between amine and benzene can significantly influence the pKa of hydrogen on NH_3^+. The separation of amines from benzene rings by aliphatic groups increases the pKa. The p*K*a value of anilinium (p*K*a ~4.6) is lower than benzylamine (p*K*a 9.34), phenethylamine (p*K*a 9.83), and makes the anilinium cation a weak base.[4] As a result, the strength of AN−H···Cl hydrogen bonding (pKa Slide Rule) can be improved in hybrid metal halides.[46,47] This will eventually result in higher penetration of organic cations into the inorganic framework. With the help of both experimental and theoretical studies, we demonstrate that the three A-site cations play a crucial role in altering the electronic structure and optical properties of 0D indium chlorides. From the density functional theory (DFT) simulation, we proved that the electronic states of these anilinium cations could directly contribute to the band edge. The use of an AN cation at the A-site and Sb^{3+} doping shows a broad yellow emission with exceptional PLQY over 90%. Interestingly, their structural and optical stability is dramatically improved in various polar and nonpolar solvents, including water. In water, they showed a reversible change with PL quenching and recovery depending on the wet and dry conditions, respectively.

RESULTS AND DISCUSSION

Single crystals of $AN_6InCl_9{\cdot}H_2O$ (AIC), $MA_4InCl_7{\cdot}H_2O$ (MIC), and $DMA_2InCl_6{\cdot}2H_2O$ (DIC) with and without Sb^{3+} doping are grown by the acid precipitation method.[48] Typically, the precursor salts are dissolved in concentrated HCl at 120 °C, and then by gradually cooling this reaction mixture at a controlled rate, the crystals of hybrid indium chlorides are obtained (see the Experimental Section for the detailed synthesis procedure). Three different anilinium salts, aniline hydrochloride (unsubstituted anilinium), 2-methyl, and 2,6-dimethyl aniline hydrochlorides are used as A-site cations. For Sb^{3+} doping, the percentage of Sb^{3+} is rationally controlled by varying the concentrations of $SbCl_3$ with respect to $InCl_3$ in the precursors. The elemental composition of Sb^{3+}-doped AIC, MIC, and DIC are obtained by inductively coupled plasma mass spectrometry (ICP-MS) and given in the supporting table (Table S1). To understand the role of the anilinium cations on properties, we have used a combination of experimental and DFT calculations and systematically investigated the crystal structure, electronic structure, optical properties, and stability.

Influence of the A-Site Cation on Crystal Packing. The crystal structures of AIC, MIC, and DIC were determined using single-crystal X-ray diffraction (SCXRD), and their crystal structures, along with XRD patterns, are shown in Figure 1. The crystal structure of AIC is shown in Figure 1a. AIC adopts a monoclinic $C12/c1$ space group with each $[InCl_6]^{3-}$ octahedron spatially isolated by six protonated aniline molecules in static orientations resulting in an electronic 0D organic−inorganic hybrid framework. As a result, a static disorder in the unit cell structure leading to a large unit cell volume (4450.2 Å^3) is observed. This static disorder could also be described as the rotational disorder, which likely resulted from the two energetically favorable orientations of aniline rings in the crystal structure. Moreover, the lattice has sufficient space to accommodate these orientations, thus leading to rotational disorder in the AIC. The closest (along the *c*-axis) distance between two $[InCl_6]^{3-}$ octahedra is 9.45 Å (Figure S1b); therefore, it rules out any indium−indium (In−In) interactions or clustering of In in the hybrid indium chlorides. Anilinium cations are packed by hydrogen bonding (NH−Cl) in the space between $[lnCl_6]^{3-}$ octahedrons.

The protonated 2-methylaniline as the A-site cation retained a similar monoclinic crystal structure to that of AIC with the $C12/c1$ space group (Figure 1b). However, unlike AIC, the MIC does not show crystal disorder, and hence crystal packing is improved, leading to a reduced unit cell volume (3523 Å^3). The presence of an additional methyl group at the *ortho* position could be preventing the disorder of anilinium cations during crystal formation. Each $[InCl_6]^{3-}$ octahedron in MIC is surrounded by four protonated 2-methylaniline molecules. Among these, two molecules show hydrogen bonding (NH−Cl) with the chloride of $[InCl_6]^{3-}$ octahedra, while the other two are forming hydrogen bonding with a water molecule (NH−O) along with uncoordinated chloride (Cl^-) ions (uncoordinated water, and Cl^- ions in Figure 1b). As a result, the nearest distance (along the *b*-axis) between $[InCl_6]^{3-}$ octahedra is reduced to 7.20 Å by a factor of 2.25 Å as compared to AIC (Figure S1c).

Unlike AIC and MIC, DIC with the 2,6-dimethyl anilinium A-site cation crystallized in a triclinic crystal system with a *P*1 space group while maintaining the 0D structure. The two methyl groups at *ortho* positions further altered the crystal structure and packing resulting in a more ordered structure with a further decrease in the unit cell volume (1134.86 Å^3). Notably, each octahedron in DIC shows the presence of a water molecule similar to that of $Cs_2InCl_5{\cdot}H_2O$ (Figure 1c), which is different in composition from AIC and MIC.[40] The space between $[InCl_5(H_2O)]^{2-}$ octahedra is occupied by two protonated 2,6-dimethyl aniline molecules stabilized by weak hydrogen bonding. Consequently, the nearest distance (along the *c*-axis) between two $[InCl_5(H_2O)]^{2-}$ octahedrons is further decreased to 7 Å (Figure S1d). Overall, with the substitution of a methyl group(s) at the *ortho* positions, we observed an increase in the crystal packing and a decrease in the distance between the octahedra. The details of the crystal refinement results for AIC, MIC, and DIC are given in the Supporting Information (Tables S2−S4). Note that all three crystals were grown using the same method, and the same B and X composition except for differences in A-site ions. Therefore, the changes in crystal packing (inter-octahedral spacing) and coordination environment (in the case of DIC) are mainly due to the increase in the number of methyl groups or the bulkiness of the A-site cations. The powder XRD patterns of AIC, MIC, and DIC were recorded and used as references for Sb^{3+}-doped AIC, MIC, and DIC hybrid indium chlorides (Figures 1d−f). The powder XRD of undoped hybrid indium chlorides matches perfectly with the simulated single-crystal XRD data. Further, the powder XRD of Sb^{3+}-doped samples

https://doi.org/10.1021/acs.chemmater.2c02737
Chem. Mater. 2022, 34, 10928−10939

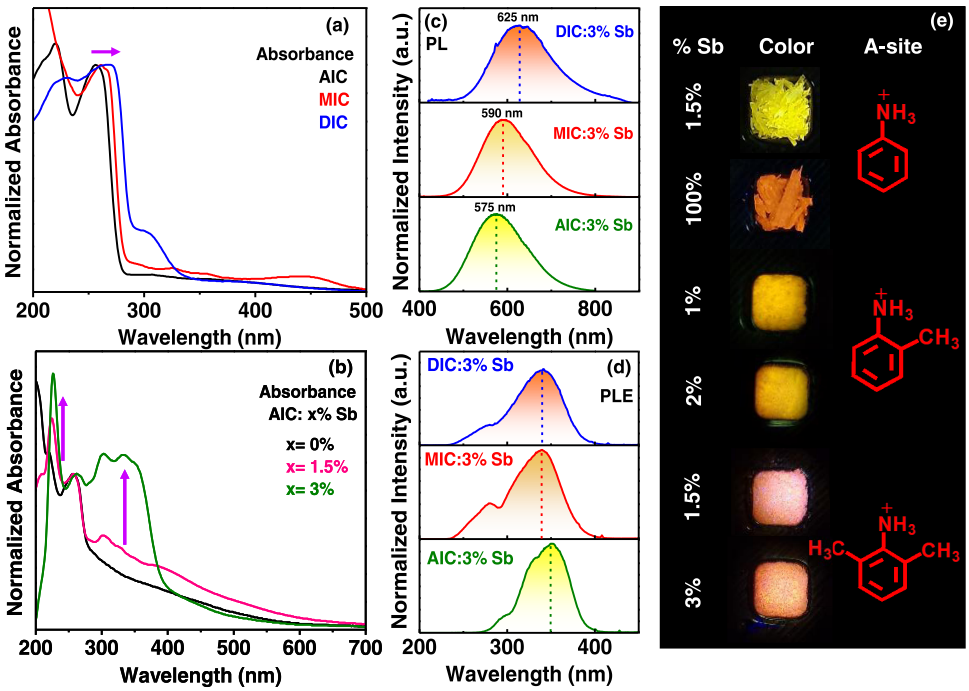

Figure 2. Optical properties of undoped and Sb^{3+}-doped 0D hybrid indium chlorides. (a) UV−visible absorption spectra of undoped AIC, MIC, and DIC. (b) UV−visible absorption spectra of Sb^{3+}-doped AIC. (c, d) Photoluminescence (PL) and photoluminescence excitation (PLE) spectra of 3% Sb^{3+}-doped AIC, MIC, and DIC. (e) Digital photographs of Sb^{3+}-doped 0D hybrid indium chlorides under 365 nm light illumination showing different colors.

matches perfectly with undoped powder XRD patterns indicating no changes in the crystal structure even after doping with Sb^{3+}. Both doped and undoped hybrid indium chlorides show the same trend in all three cases (AIC, MIC, and DIC). The similarity in the XRD patterns might be attributed to the resemblance in the ionic radii of Sb^{3+} (0.76 Å) and In^{3+} (0.8 Å) for six coordination. To further validate that Sb^{3+} is incorporated as a dopant ion instead of crystallizing separately to form pure $[A_3SbCl_5]\cdot H_2O$ (A = AN, MA, and DMA) hybrid antimony chlorides, we synthesized pure (100%) Sb-chlorides using the same method and recorded the powder XRD patterns. The top panel (shown in green lines) of Figure 1d−f are powder XRD patterns of pure antimony chlorides. From these figures, we observe no overlap in the diffraction peaks between pure hybrid antimony chlorides and Sb^{3+}-doped hybrid indium chlorides, confirming the successful Sb^{3+} incorporation in hybrid indium chlorides instead of crystallizing as hybrid antimony chloride with a 0D structure; this agrees with existing reports.[49] The powder XRD patterns of samples doped with various Sb^{3+} loadings (1.5 and 2%) show the same diffraction patterns as 3% Sb^{3+}-doped hybrid indium chlorides (Figure S2).

Impact of A-Site Cations on Optical Properties. After the structural analysis, we turned to determine the optical properties by recording UV−visible absorption spectra of both doped and undoped AIC, MIC, and DIC hybrid indium chlorides. The UV−visible absorption spectra normalized at ∼255 nm of undoped samples are shown in Figure 2a. A modest red shift in the absorption spectra, with peaks positioned at 255, 262, and 268 nm for AIC, MIC, and DIC, respectively, is observed. Although the magnitude of the red-shift is small, it systematically increases with the increase in the number of methyl groups on the A-site cation. The transitions corresponding to these absorption maxima are primarily localized on inorganic octahedra $[InCl_6]^{3-}$.[50] Therefore, the shift in the peak position indicates subtle changes in the position of VB and CB and might be resulting from structural changes with changes in the A-site cation.

Figure 2b compares the optical absorption of undoped and Sb^{3+}-doped AIC. The Sb^{3+}-doping induces a new absorption shoulder at 350 nm. With an increase in Sb^{3+} loading, the intensity of the 350 and 255 nm peaks increases (purple upward arrows, Figure 2b). The absorption shoulder at 350 nm is generally assigned to partially allowed electronic transition from the $^1S_0$ ground state to the $^3P_1$* excited state. Since Sb^{3+} has $5s^2$ outer electrons, in the free ionic state, $^1S_0$ is the ground state while $^1P_1$ and $^3P_{n(n=0,1,2)}$ are excited states.[13,39,51] Note that $^3P_1$* is a relaxed excited state resulting from the spin-orbit coupling of $^1P_1$ and $^3P_1$ states.[40] This $^1S_0 \rightarrow {}^3P_1$* electronic transition can also be defined using Mulliken symbols as $^1A_{1g} \rightarrow {}^3T_{1u}$* when Sb^{3+} is considered in the cubic crystal field.[52,53] Similar trends in absorbance were observed when Sb^{3+}-doping is increased in MIC and DIC (Figure S3a,b); however, the magnitude of the increase in the absorbance is different for each hybrid indium chloride.

Further, the emission spectra were recorded under steady-state illumination at various excitation wavelengths. Undoped samples show no emission spectra at room temperature regardless of the excitation energy and A-site cations. Note that the transitions in In-halides are parity forbidden, thus showing weak emission and poor PLQYs.[33] After doping with Sb^{3+}, all AIC, MIC, and DIC show intense broadband emission across the visible region (Figure 2c and S4). Such broadband emission by breaking the forbidden transitions in In through Sb has been assigned to the $^3P_1$* → $^1S_0$ transition (triplet STE) and was previously observed in various Sb^{3+}-doped 0D metal halides.[33,13,39,40,52] Furthermore, we recorded PL excitation (PLE) spectra and observed all hybrid indium

https://doi.org/10.1021/acs.chemmater.2c02737
Chem. Mater. 2022, 34, 10928−10939

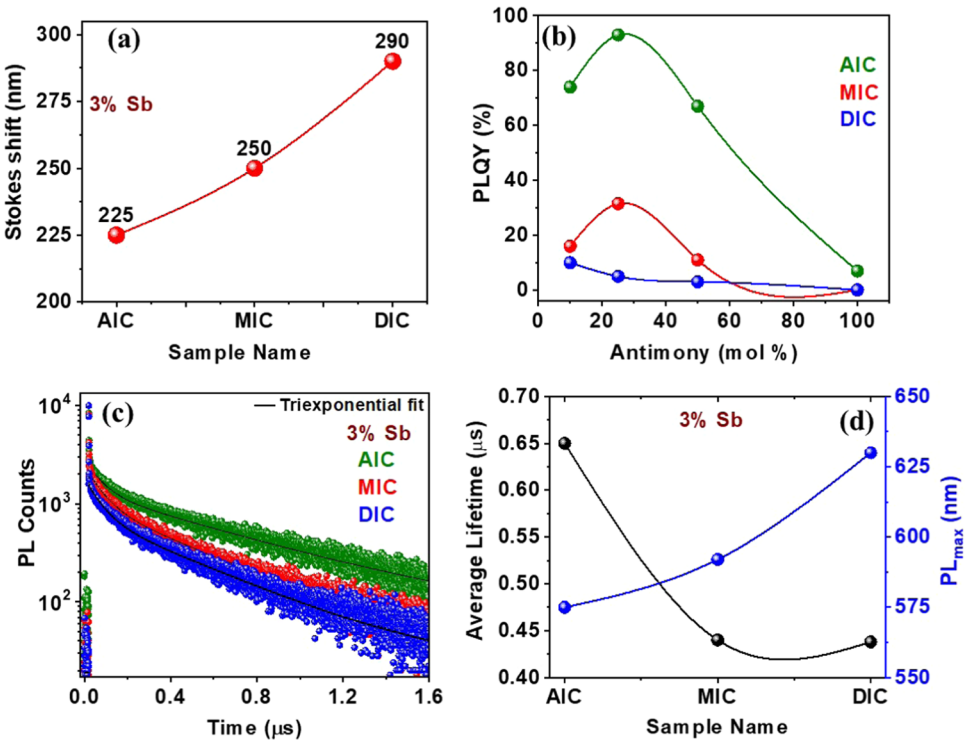

Figure 3. Comparative analysis of optical properties. The systematic changes in the (a) Stokes shift, (b) photoluminescence quantum yield (PLQY), (c, d) time-resolved PL decay dynamics with an increase in the ortho-substitutions of A-site cations in AIC, MIC, and DIC. The connecting lines in a, b, and d are drawn just to guide the reader (not fitting).

chloride crystals showing the PLE peak at around ∼350 nm (350 nm AIC, 345 nm MIC, and 345 nm DIC). As expected, the PLE spectra show a perfect overlap with the absorption spectra (Figures 2b,d and S5). Interestingly, the PL characteristics such as the PL quantum yields, full-width at half maximum (FWHM), PL peak position, and Stokes shift, are highly dependent on the type of A-site cation. Note that, in addition to the A-site cation, the percentage loading of Sb^{3+} also played a role in PL quantum yields of hybrid indium chlorides (discussed later). Figure 2c shows PL spectra of 3% Sb^{3+}-doped AIC, MIC, and DIC, where the PL spectra are systematically red-shifted with an increase in methyl groups on A-site anilinium ions. As discussed earlier increased methyl group substitution resulted in significant changes in the crystal packing. However, a change in the crystal packing may or may not have significant effects on the PL unless it alters the geometry of $[SbCl_5]^{2-}$ centers since the frontier orbitals are localized on Sb and Cl. The origin of PL changes is discussed in detail using DFT and PDOS analysis. AIC (no methyl group on the A-site cation) shows a PL at 575 nm with an FWHM of 143 nm. Whereas, 2-methyl (MIC) and 2,6-dimethyl (DIC) substituted hybrid indium chlorides show broad emission spectra centered at 590 nm (red-shifted by 15 nm) with a FWHM of 135 nm and 625 nm (red-shifted by 50 nm) with a FWHM of 156 nm, respectively. As a result of the red shift in PL with variations in the FWHM, hybrid indium chlorides exhibit various emission colors such as pink, yellow, and orange with a change in the A-site cation (Figure 2e). The interactions between organic A-site cations and inorganic octahedra are generally assigned to hydrogen bonding and van der Waals interaction between the NH_3^+ and Cl^- ions.[54,55] With the increase in methyl substitution on the A-site cation, the magnitude of NH−Cl interactions is possibly affected since the orientation of organic cations and inter-octahedral spacing are significantly different in each hybrid indium halide crystal. Therefore, these interactions can facilitate the penetration of organic cations into the inorganic framework proximity and warrant the A-site cations in governing the optical properties. However, to inspect these changes in absorption and emission, we performed DFT computations and discussed them in the later sections.

In Figure 3, we summarize all the results of steady-state PL and compare them with time-resolved PL spectra for 3% Sb^{3+}-doped AIC, MIC, and DIC. Figure 3a shows a significant increase in the Stokes shift, primarily due to the red shift in the emission peak. In addition to the Stokes shift, the PLQYs are dramatically affected by the type of A-site cations used in hybrid indium chlorides. Figure 3b shows PLQYs of AIC, MIC, and DIC plotted against Sb^{3+} loading. Note that to simplify the plot, the Sb^{3+} amounts in Figure 3b are represented in precursor antimony amounts (mol %), where the peak PLQY values correspond to 2, 2.5, and 2% of actual Sb^{3+} amounts for AIC, MIC, and DIC, respectively (refer to ICP-MS data Table S1). The PLQY of AIC and MIC follows the same trend with respect to the amount of Sb^{3+}, where the PLQY is increased with an increase in the Sb^{3+} amount, and then decreases with a further increase in Sb^{3+} loading after reaching a maximum value for ∼2% Sb^{3+} (25 mol %). Whereas the PLQYs of Sb^{3+}-doped DIC show a linear relation to the Sb^{3+} amount with low efficiencies. The highest PLQY of 93% is observed for 2% Sb^{3+}-doped AIC, which is ∼30% for 2.5% Sb^{3+} MIC and ∼10% for 2% Sb^{3+}-doped DIC. The PLQYs are decreasing with an increase in the number of methyl groups on anilinium cations. Consequently, PL decay profiles were recorded at the emission maxima for 3% Sb^{3+}-doped AIC, MIC, and DIC, and a systematic decrease in the average

https://doi.org/10.1021/acs.chemmater.2c02737
Chem. Mater. 2022, 34, 10928−10939

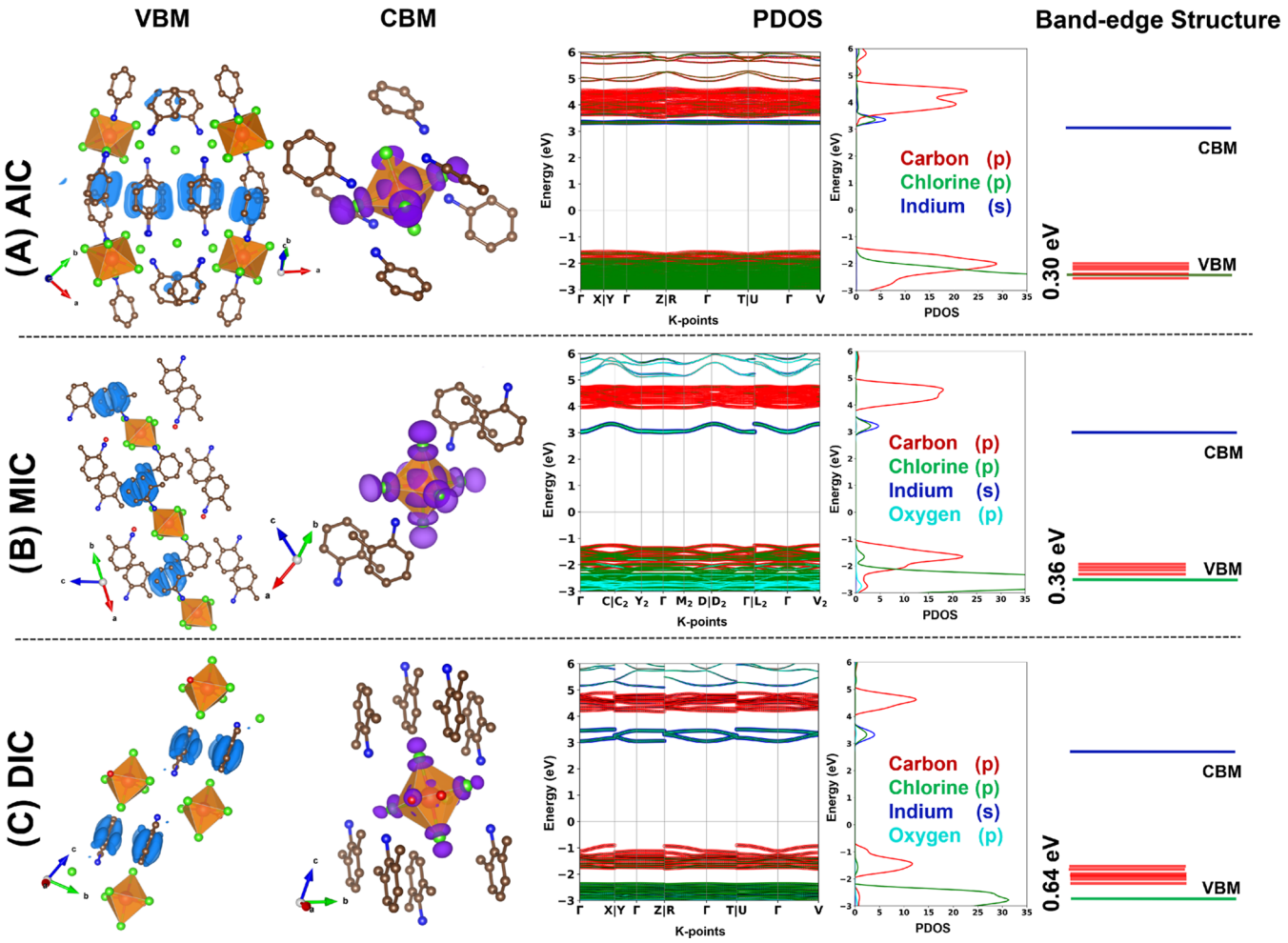

Figure 4. Electronic structure of 0D hybrid indium chlorides from DFT analyses. (A) AIC, (B) MIC, and (C) DIC panels represent simulation results for anilinium, 2-methyl anilinium, and 2,6-dimethyl anilinium containing indium chlorides. The left two columns show distribution of the VBM on organic A-site cations, and CBM on inorganic octahedra. The central two columns represent the partial density of states (PDOS), showing the contribution of carbon p-orbitals from A-site cations near the band edge. The right most column schematic representation of the band-edge contribution of A-site cations with an upward shift near the VBM as the number of methyl groups increase on the A-site.

lifetimes (Figure 3c,d) with an increase in methyl groups is observed. This is in alignment with the trend in PLQYs. We fit the decay profile to tri-exponential and the best-fit parameters are given in Table S5. The average lifetimes derived from the fitting are 0.65, 0.44, and 0.45 μs, respectively, for AIC, MIC, and DIC (3% Sb^{3+} doped). The decrease in lifetimes and PLQYs with an increase in methyl groups on the A-site cation suggest that the methyl groups contribute to nonradiative decay channels. This could be attributed to either vacancy in hybrid indium chlorides or the delocalization of excitons.[56] We also note that with increasing methyl substitution, there is a significant change in the crystal packing due to the change in stoichiometry. These structural changes may also lead to observed differences in the optical properties of metal halides.

To gain fundamental insights into the change in optical properties with methyl substitution on A-site cations, we computed band structures using density functional theory (DFT) with the hybrid HSE06 functional on both undoped and Sb^{3+}-doped hybrid indium chlorides. The frontier orbitals and the electronic band structure are shown in Figure 4. There is an indirect band gap for AIC (Y → Γ), MIC(L_2 → Γ), and DIC (U → Γ) with values of 4.9, 4.3, and 4.0 eV, respectively (Figure 4). The reduction in the band gap with an increase in the methyl substitution on the A-site cation agrees well with the measured red shift in the absorption peaks (Figure 2a). While comparing the partial band structure and density of states (PDOS) (Figure 4A, central two columns), we observe a large overlap between the p-orbitals of carbon (C) and chlorine (Cl) atoms at the VBM in AIC. In MIC and DIC additional methyl groups at the respective *ortho* positions shift the carbon p-orbitals upward into the band gap and lead to a reduction in the p-orbital overlap unlike the case in AIC (Figure 4B and C, central two columns). Interestingly, despite the metal−oxygen bond in the case of DIC, the oxygen (p) orbitals showed almost negligible contribution near the band edge. The VBM is composed of Cl^- ions, therefore the shift in the VBM with the change in A-site cations is an indication of stronger penetration of A-site cations via interacting with Cl^- of the inorganic octahedron.

From the frontier orbital picture in Figure 4 (left two columns), the VBM is largely localized on organic A-site cations while the CBM is predominantly composed of the B-site indium ion. The upward shift of the VBM with methyl substitution eventually resulted in a smaller band gap of DIC, and MIC compared to AIC. The magnitude of the upward shift in the p-orbital of C compared to Cl atoms at the VBM was

https://doi.org/10.1021/acs.chemmater.2c02737
Chem. Mater. 2022, 34, 10928−10939

found to be 0.30, 0.36, and 0.64 eV for AIC, MIC, and DIC, respectively, as illustrated in Figure 4 (right column). DFT calculations confirm a noticeable contribution of organic A-site cations to the VBM.

Next, we investigated the role of the Sb^{3+} dopant in AIC, MIC, and DIC systems to delineate the effect of doping on PL dynamics. From the band structure of Sb^{3+}-doped AIC, MIC, and DIC, we observe 5s and 5p orbitals of Sb^{3+} contributing strongly to the VB and CB with 5s to band-edge states near the VBM (Figure S7). The full band structure of doped and undoped AIC, MIC, and DIC is given in Figure S8. To examine the effect of low doping concentration, we calculate the projected density of states (PDOS) at the PBE level for the $2 \times 2 \times 2$ supercell of Sb^{3+}-doped AIC, MIC, and DIC and compare it with the unit cell calculations. As can be seen from Figure S9, both the PDOS are very similar with a peak of Sb *s*-orbital at the valance band edge. This suggests that our considered models with 50% doping concentration do capture the effect of Sb^{3+}-doping qualitatively. Importantly, the contribution from carbon p-orbitals near the VBM increases from AIC to DIC resulting in partial or complete overlap of 5s orbitals of Sb^{3+} and p-orbital of carbon in MIC and DIC. We do not observe significant changes in the relative positions of Sb and Cl orbitals, instead, we observed an increase in C (p) orbital contribution near the VB edge. Corresponding C (p) orbitals shifted upward toward the edge as the A-site cation changes from anilinium to dimethyl anilinium. In the case of Sb^{3+}-doped DIC, the VBM is evidently dominated by C (p) orbitals as shown in Figures S7 and S9, and are considered responsible for the red-shift in PL. Therefore, a change in crystal packing has a significantly lower impact on the bonding environment and the PL changes are considered to be dependent on the change in C (p) contribution at the VBM. The Sb^{3+}-doping in AIC yields an almost flat valance band due to a strong hybridization between Sb 5s-orbital and Cl 3p-orbital, resulting in a very high hole effective mass (m_h^* = 311.3 m_0, where m_0 is the resting mass of an electron) compared to pristine AIC (5.3 m_0). Moreover, the electron effective mass (m_e^*) for the pristine and doped AIC is 9.0 m_0 and 62.4 m_0, respectively (Table 1). In contrast, we observe a marginal decrease in the m_h^* in Sb^{3+}-doped MIC and DIC probably due to the weakening of the s−p overlap of Sb and Cl atoms at the VBM. The values of m_e^* for Sb^{3+}-doped MIC, and DIC were found to be 156.4 m_0 and 14.7 m_0, respectively, which are still higher than their undoped counterparts. Further, we derived the reduced effective masses using $\mu = m_e^* m_h^* / (m_e^* + m_h^*)$, which were found to be 52.0, 5.4, and 1.5 respectively, for Sb^{3+}-doped AIC, MIC, and DIC (Table 1). The decrease in reduced mass means an increase in carrier mobility (carrier confinement is decreasing) from AIC to DIC. Interestingly, the trend in μ values is in alignment with the trend observed in PLQY where AIC, MIC, and DIC showed PLQYs of 93, 31.5, and 5%, respectively, and can be correlated with the increased carbon p-orbital contribution near the VBM. A high PLQY with a large effective mass in AIC suggests that poor carrier mobility (strong exciton binding) is responsible for high radiative recombination rates. Similarly, low PLQY in DIC and small effective mass indicate that the excitons generated on octahedron centers are delocalized and decaying nonradiatively with a faster decay. It must be noted that in addition to the carbon (p) contribution there is a significant reduction in the distance between octahedral centers in AIC—9.45 Å, MIC—7.20 Å, and DIC—7.00 Å, (Figure S1b−d), which could also lead to the reduced effective mass of charge carriers and thus could impact the optical properties. PDOS/DFT data alone cannot quantify the accurate contribution of each of these effects. To get more insight into realistic contributions either from A-site cations or structural or stoichiometric changes and their consequences on optical properties, further studies on maybe more combinations of A-site and BX octahedra, are warranted.

Table 1. Comparison of the Electronic Band Gap (in Units eV), the Effective Mass of Electrons/Holes (m_e^*/m_h^*), and Reduced Mass (μ) of AIC, MIC, and DIC and Their Corresponding Sb^{3+}-Doped Counterparts

	band gap [E_{gap} (eV)]			effective mass (in units of m_0)		reduced Mass
systems	PBE	HSE06	transitions	m_e^*	m_h^*	$\mu = \frac{m_e^* m_h^*}{(m_e^* + m_h^*)}$
AIC	3.9	4.9	Y → Γ	9.0	5.3	3.3
MIC	3.3	4.3	L_2 → Γ	1.3	5.9	1.1
DIC	3.0	4.0	U → Γ	2.9	2.5	1.3
Sb-AIC	3.1	4.1	Y → Y	62.4	311.3	52.0
Sb-MIC	2.9	3.9	R → Z	156.4	5.6	5.4
Sb-DIC	3.1	4.1	Y → Y	14.7	1.7	1.5

Further, we subjected Sb^{3+}-doped AIC, MIC, and DIC to various (polar and nonpolar) solvents, including water, toluene, hexane, ethyl acetate, and ethanol, for over 20 days to test their stability. Figure 5a shows the digital photographs of 3% Sb^{3+}-doped AIC crystals in various solvents taken on days 1 and 22. Bright yellow emission of AIC is preserved even after soaking for 22 days in most of the solvents. Notably, the PL spectra have no shift in the emission maximum and spectral pattern until day 22 (Figure S10). However, in water, the emission intensity is gradually decreased, with complete PL quenching after an hour of soaking (Figure S11a). The quenching of PL in water is observed in all hybrid indium chlorides, however, with a slight variation in quenching times. To understand the extent of water stability, we performed repeated experiments of drying and wetting hybrid indium chlorides in water. Surprisingly, the PL recovered back after each drying cycle without any changes in their spectral pattern (Figure 5b). The PL is sustained for 6 cycles; however, the spectral intensity decreased systematically after each cycle. Interestingly, from powder XRD analysis, we discovered that the crystal structure is preserved with no significant changes in the characteristic diffraction peaks even after soaking for 21 days in water (Figure 5c). Note that this yellow emission in Sb^{3+}-doped AIC originates from transitions in Sb; therefore, the repeated emission quenching and recovery without affecting the crystal structure indicates that the water molecules are interacting with the Sb sites by acting as PL quenchers without their chemical decomposition. The energy transfer from Sb^{3+} states to water requires rigorous spectroscopic studies. Similarly, 3% Sb^{3+}-doped MIC and DIC showed optical and structural stability in different solvents, including water (Figures S11b,c, S12, and S13), which perhaps could be attributed to the strong $\pi-\pi$ interactions of the benzene rings in anilinium cations.

CONCLUSIONS

In summary, we showed that by rationally engineering the A-site cation interactions with the inorganic $[BX]_6^{2-}$ framework,

https://doi.org/10.1021/acs.chemmater.2c02737
Chem. Mater. 2022, 34, 10928−10939

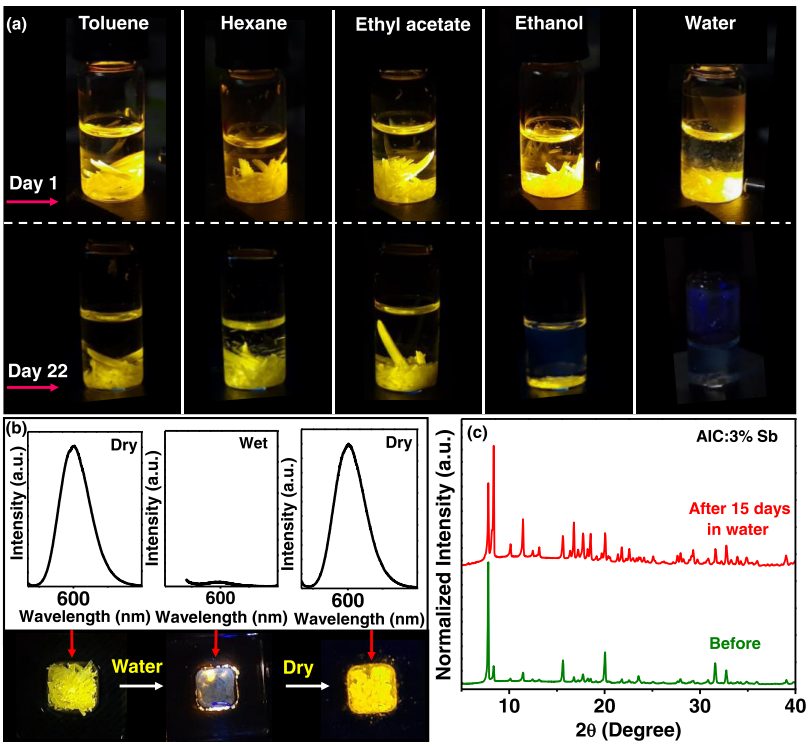

Figure 5. Stability of 0D hybrid indium chlorides. (a) Digital photographs of 3% Sb^{3+}-doped AIC soaked in various polar and nonpolar solvents. The pictures are taken on the first and 22nd day of soaking. (b) PL spectra of the dry−wet−dry cycle. The lower panel shows digital photographs of samples under dry and wet conditions under the illumination of UV light (365 nm). (c) Powder XRD patterns of the 3% Sb^{3+}-doped AIC before soaking in the water and after soaking for 15 days in water.

the band-edge contribution of A-site cations is improved and demonstrated the critical role of A-site cations in governing their optical and electronic properties. By changing A-site cations in hybrid indium chlorides, the emission spectra are tuned across the wavelengths in visible regions to produce yellow, orange, and pink crystals. Moreover, hybrid indium chlorides with very high PLQYs over 93% and low <10% are achieved by increasing methyl groups on A-site cations. With the help of DFT calculations, we found that the low PLQYs in dimethyl-substituted anilinium indium chlorides are attributed to the delocalization of exciton owing to their decreased effective mass. This is also supported by the distribution of the frontier orbitals across organic and inorganic moieties. In addition to the orbital delocalization, we observed significant changes in the crystal packing that could affect optical properties as well. Finally, we demonstrated the remarkable stability of hybrid indium chlorides in various solvents. In water, the Sb^{3+}-doped hybrid indium chlorides showed compelling PL recovery after drying. This was reversible for several dry−wet cycles. Overall, by showing the critical role of A-site cations, this work demonstrates the enormous potential of A-site cations in tuning the properties beyond the stabilization of the structure.

EXPERIMENTAL SECTION

Materials. Aniline (≥99.5%), 2-methylaniline (≥99%), 2,6-dimethyl aniline (99%), hydrochloric acid (HCl; 37 wt % in H_2O), indium(III) chloride ($InCl_3$; 98%), antimony(III) chloride ($SbCl_3$; ≥99.95%), and nitric acid (HNO_3; 70%) are purchased from Sigma-Aldrich. All chemicals are used as received without further purification.

Methods. *Preparation of Hydrochloride Salts of AN, MA, and DMA.* Aniline (AN), 2-methylaniline (MA), and 2,6-dimethyl aniline (DMA) (1 mmol of each) are taken separately in three different 15 mL glass vials and placed in an ice water bath for cooling. After 10 min, 3 mL of HCl is slowly added to each glass vial, and vials are kept undisturbed for additional 10 min. White precipitate with cloudy gas forms immediately after HCl addition. Subsequently, a white precipitate is collected by filtration and used for the next step after drying.

Synthesis of $AN_6InCl_9{\cdot}H_2O$ (AIC) Single Crystals. For single-crystal growth of AIC, a glass vial is loaded with hydrochloride salt of AN (2 mmol), $InCl_3$ (1 mmol), and 7 mL of HCl. A glass vial containing the above mixture is placed in an oil bath and heated using a hot plate at 100 °C with vigorous stirring. The temperature of the oil is monitored by a thermometer. After the complete dissolution of the precursors, heating is stopped, and the reaction mixture is allowed to cool to room temperature. The reaction mixture shows the formation of white crystals. White crystals of $AN_6InCl_9{\cdot}H_2O$ are filtered by vacuum filtration using a Buchner funnel attached to the Erlenmeyer flask. The final product is dried in a vacuum desiccator and stored in a glass vial.

Synthesis of $MA_4InCl_7{\cdot}H_2O$ (MIC) and $DMA_2InCl_6{\cdot}2H_2O$ (DIC) Single Crystals. The procedure for the synthesis of $MA_4InCl_7{\cdot}H_2O$ (MIC) and $DMA_2InCl_6{\cdot}2H_2O$ (DIC) single crystals is the same as described for AIC. Except for MIC, precursors are dissolved in 3 mL of HCl instead of 7 mL. To obtain white crystals, the reaction mixture is cooled below room temperature in a refrigerator (∼5 °C) for 1 hr.

Sb^{3+}-doped single crystals are also formed by following the above procedure except for the addition of $SbCl_3$ (0.25, 0.5, and 1 mmol) along with the above-listed precursors. Please note that for a reaction with 1 mmol of $SbCl_3$, the reaction mixture does not contain $InCl_3$. The synthesis procedure is schematically given in Supporting Material as Scheme 1.

Stability Tests. Dry−wet−dry cycles are carried out by filling samples in quartz. PL of the sample is measured before adding water. Once water (0.5 mL) is added to the sample (∼40 mg), the measurement is started by setting an automatic PL recording for every 1 min using ocean view software. After complete emission quenching (intensity comes close to zero), measurement is stopped. Sub-

https://doi.org/10.1021/acs.chemmater.2c02737
Chem. Mater. 2022, 34, 10928−10939

sequently, the sample containing quartz is placed on a hot plate (set at 80 °C) for drying. After 1 h of heating at 80 °C, the sample shows intense yellow emission when illuminated with a 365 nm UV torch. The above process is repeated six times using the same sample to understand the optical recovery in water. To understand the stability of various solvents, samples were soaked for 21 days, and everyday PL spectra were recorded.

MEASUREMENTS AND CHARACTERIZATION

The single-crystal X-ray diffraction (SCXRD) data are measured at 100 K, using a three circles goniometer Kappa geometry with a Chi fixed angle at 54.74° Bruker AXS D8 Venture, equipped with a Photon 100 CMOS active pixel sensor detector. A monochromatized Cu X-ray radiation (λ = 1.54178 Å) was selected for the measurement. All frames were integrated with the aid of the Bruker SAINT software using a narrow-frame algorithm. Crystals are solved and refined using the Bruker SHELXT Software Package, refinement of the structure was carried out by least-squares procedures on weighted F^2 values using SHELXTL-2018/3 included in the APEX4 v2021, 4.0, AXS Bruker program. The crystal structure visualization and interpretation was done using VESTA software.[57] Powder XRD is recorded using PROTO, AXRD benchtop powder diffraction system equipped with Cu Kα (1.54 Å) radiation. Elemental analysis is carried out using a Perkin Elmer SCIEX, Elan DRC II inductively coupled plasma mass spectrometer (ICP-MS). Diffuse reflectance spectra are recorded using a Shimadzu UV-2600i UV−visible spectrophotometer. Kubelka−Munk transformation is used for the analysis of diffuse reflectance spectra.[58] The following equation (eq 1) gives the relation between reflectance data and absorption coefficient

$$F(R) = \alpha/s = (1 - R)^2/2R \quad (1)$$

where $F(R)$ is the Kubelka−Munk function, R is the reflectance, α is the absorption coefficient, and s is the scattering factor. Steady-state photoluminescence (PL) and PL excitation (PLE) spectra are measured using an Edinburgh FS5 spectrofluorometer. Time-resolved photoluminescence (TRPL) measurements are carried out using the Deltaflex modular fluorescence lifetime system, Horiba Scientific equipped with a 356 nm LED source. For photoluminescence quantum yield (PLQY) measurement, an integrated sphere calibrated against the Newport photodetector is used. Samples are illuminated with a 365 nm LED (Thorlabs). For accuracy, the PLQY measurements are carried out by the following method reported by Mello et al.[59] Powder samples are filled in a capillary tube and loaded into a quartz cuvette for PLQY measurements. All digital photographs are taken using Samsung M30S mobile camera.

Computational Methods. All the computations were carried out using the density functional theory (DFT)[60,61] with the projector-augmented-wave (PAW) method[61−63] as implemented in the Vienna Ab initio Simulation Package (VASP)[62−64] software. Contributions from the exchange−correlation interaction are accounted for using the Perdew−Burke−Ernzerhof (PBE) functional within the generalized gradient approximation (GGA).[65] A kinetic energy cutoff of 450 eV is used to generate a plane-wave basis set. To sample Brillouin Zone a 2 × 2 × 3, 4 × 4 × 1, and 3 × 2 × 2 γ-centered k-points mesh is used for $AN_6InCl_9{\cdot}H_2O$ (AIC), $MA_4InCl_7{\cdot}H_2O$ (MIC), and $DMA_2InCl_6{\cdot}2H_2O$ (DIC), respectively. For the geometry optimization, threshold values for self-consistent field (SCF) energies and residual forces on each atom are set as 10^{-6} and 0.02 eVÅ^{-1}, respectively. To evaluate accurate band gap values hybrid Heyd−Scuseria−Ernzerhof 2006 (HSE06) functional with 25% Hartree−Fock exact exchange (α = 0.25) is employed.[66] Achieving an experimental doping concentration of 3% would require a supercell that is 17 times bigger than the current system size making these calculations intractable. Thus, a single In atom is replaced with Sb yielding a dopant concentration of 50%, which is significantly larger than the experiment but allows us to explain experimental trends qualitatively.

ASSOCIATED CONTENT

Supporting Information

The Supporting Information is available free of charge at https://pubs.acs.org/doi/10.1021/acs.chemmater.2c02737.

Experimental procedure, characterization details, absorption, PL, PLE, XRD, TRPL data (PDF)

Computational data (CIF)

Data for stability tests and single-crystal refinement data (CIF)

CCDC Single-crystal deposition numbers are 2175612, 2175613, and 2175614 for AIC, MIC, and DIC respectively (CIF)

AUTHOR INFORMATION

Corresponding Authors

Neeraj Rai − *Dave C. Swalm School of Chemical Engineering and Center for Advanced Vehicular Systems, Mississippi State University, Mississippi State, Mississippi 39762, United States;* orcid.org/0000-0002-0058-9623; Email: neerajrai@che.msstate.edu

Mahesh K. Gangishetty − *Department of Chemistry and Department of Physics and Astronomy, Mississippi State University, Mississippi State, Mississippi 39762, United States;* orcid.org/0000-0002-1680-1457; Email: mgangishetty@chemistry.msstate.edu

Authors

Anuraj S. Kshirsagar − *Department of Chemistry, Mississippi State University, Mississippi State, Mississippi 39762, United States*

Yashpal Singh − *Dave C. Swalm School of Chemical Engineering and Center for Advanced Vehicular Systems, Mississippi State University, Mississippi State, Mississippi 39762, United States;* orcid.org/0000-0003-0431-1079

Udara M. Kuruppu − *Department of Chemistry, Mississippi State University, Mississippi State, Mississippi 39762, United States*

Bruno Donnadieu − *Department of Chemistry, Mississippi State University, Mississippi State, Mississippi 39762, United States*

Complete contact information is available at: https://pubs.acs.org/10.1021/acs.chemmater.2c02737

Author Contributions

A.S.K. and U.M.K. synthesized crystals, A.S.K. performed all characterizations of crystals. Y.S. performed DFT calculations, associated analysis, and wrote the computational sections of the initial draft. The single-crystal XRD data were analyzed by crystallographer B.D. M.K.G. and N.R. supervised the project,

https://doi.org/10.1021/acs.chemmater.2c02737
Chem. Mater. 2022, 34, 10928−10939

the first draft was written by A.S.K. and all the authors contributed equally to editing and revising the manuscript.

Funding

(1) NSF Track 1 EPSCoR funding grant no. 1757220 and (2) SRI seed fund from Mississippi State University.

Notes

The authors declare the following competing financial interest(s): Mississippi State University is filing a provisional patent on this work.

■ ACKNOWLEDGMENTS

The work has been supported by the National Science Foundation (NSF). We acknowledge the support of NSF funding under the grant no. OIA-1757220. We would like to thank Prof. Santanu Kundu for kindly allowing us to use their Edinberg PL/PLE setup. MKG and ASK are thankful for the SRI seed grant supported by the Mississippi State University for the lab-supply support. This work used the Extreme Science and Engineering Discovery Environment (XSEDE), which is supported by the National Science Foundation grant number ACI-1548562.[67] Y.S. and N.R. acknowledge the Texas Advanced Computing Center (TACC) at The University of Texas at Austin for providing high performance computing resource (Stampede 2) through an XSEDE allocation: CHE140141. Part of this work was performed on computational resources at the High Performance Computing Collaboratory (HPC2) at Mississippi State University.

■ REFERENCES

(1) Nedelcu, G.; Protesescu, L.; Yakunin, S.; Bodnarchuk, M. I.; Grotevent, M. J.; Kovalenko, M. V. Fast anion-exchange in highly luminescent nanocrystals of cesium lead halide perovskites ($CsPbX_3$, X = Cl, Br, I). *Nano Lett.* **2015**, *15*, 5635−5640.

(2) Buin, A.; Comin, R.; Xu, J.; Ip, A. H.; Sargent, E. H. Halide-dependent electronic structure of organolead perovskite materials. *Chem. Mater.* **2015**, *27*, 4405−4412.

(3) Saliba, M.; Matsui, T.; Seo, J.-Y.; Domanski, K.; Correa-Baena, J.-P.; Nazeeruddin, M. K.; Zakeeruddin, S. M.; Tress, W.; Abate, A.; Hagfeldt, A.; Grätzel, M. Cesium-containing triple cation perovskite solar cells: improved stability, reproducibility and high efficiency. *Energy Environ. Sci.* **2016**, *9*, 1989−1997.

(4) Dey, A.; Ye, J.; De, A.; Debroye, E.; Ha, S. K.; Bladt, E.; Kshirsagar, A. S.; Wang, Z.; Yin, J.; Wang, Y.; Quan, L. N.; Yan, F.; Gao, M.; Li, X.; Shamsi, J.; Debnath, T.; Cao, M.; Scheel, M. A.; Kumar, S.; Steele, J. A.; Gerhard, M.; Chouhan, L.; Xu, K.; Wu, X.-g.; Li, Y.; Zhang, Y.; Dutta, A.; Han, C.; Vincon, I.; Rogach, A. L.; Nag, A.; Samanta, A.; Korgel, B. A.; Shih, C.-J.; Gamelin, D. R.; Son, D. H.; Zeng, H.; Zhong, H.; Sun, H.; Demir, H. V.; Scheblykin, I. G.; Mora-Seró, I.; Stolarczyk, J. K.; Zhang, J. Z.; Feldmann, J.; Hofkens, J.; Luther, J. M.; Pérez-Prieto, J.; Li, L.; Manna, L.; Bodnarchuk, M. I.; Kovalenko, M. V.; Roeffaers, M. B. J.; Pradhan, N.; Mohammed, O. F.; Bakr, O. M.; Yang, P.; Müller-Buschbaum, P.; Kamat, P. V.; Bao, Q.; Zhang, Q.; Krahne, R.; Galian, R. E.; Stranks, S. D.; Bals, S.; Biju, V.; Tisdale, W. A.; Yan, Y.; Hoye, R. L. Z.; Polavarapu, L. State of the art and prospects for halide perovskite nanocrystals. *ACS Nano* **2021**, *15*, 10775−10981.

(5) Hou, S.; Gangishetty, M. K.; Quan, Q.; Congreve, D. N. Efficient blue and white perovskite light-emitting diodes via manganese doping. *Joule* **2018**, *2*, 2421−2433.

(6) Manser, J. S.; Christians, J. A.; Kamat, P. V. Intriguing optoelectronic properties of metal halide perovskites. *Chem. Rev.* **2016**, *116*, 12956−13008.

(7) Protesescu, L.; Yakunin, S.; Bodnarchuk, M. I.; Krieg, F.; Caputo, R.; Hendon, C. H.; Yang, R. X.; Walsh, A.; Kovalenko, M. V. Nanocrystals of cesium lead halide perovskites ($CsPbX_3$, X = Cl, Br, and I): Novel optoelectronic materials showing bright emission with wide color gamut. *Nano Lett.* **2015**, *15*, 3692−3696.

(8) Jellicoe, T. C.; Richter, J. M.; Glass, H. F. J.; Tabachnyk, M.; Brady, R.; Dutton, S. E.; Rao, A.; Friend, R. H.; Credgington, D.; Greenham, N. C.; Böhm, M. L. Synthesis and optical properties of lead-free cesium tin halide perovskite nanocrystals. *J. Am. Chem. Soc.* **2016**, *138*, 2941−2944.

(9) Chen, L.-J. Synthesis and optical properties of lead-free cesium germanium halide perovskite quantum rods. *RSC Adv.* **2018**, *8*, 18396−18399.

(10) Huang, J.; Lei, T.; Siron, M.; Zhang, Y.; Yu, S.; Seeler, F.; Dehestani, A.; Quan, L. N.; Schierle-Arndt, K.; Yang, P. Lead-free cesium europium halide perovskite nanocrystals. *Nano Lett.* **2020**, *20*, 3734−3739.

(11) Pal, J.; Manna, S.; Mondal, A.; Das, S.; Adarsh, K. V.; Nag, A. Colloidal synthesis and photophysics of $M_3Sb_2I_9$ (M=Cs and Rb) nanocrystals: Lead-free perovskites. *Angew. Chem., Int. Ed.* **2017**, *56*, 14187−14191.

(12) Zhou, L.; Xu, Y. F.; Chen, B. X.; Kuang, D. B.; Su, C. Y. Synthesis and photocatalytic application of stable lead-free $Cs_2AgBiBr_6$ perovskite nanocrystals. *Small* **2018**, *14*, No. 1703762.

(13) Arfin, H.; Kshirsagar, A. S.; Kaur, J.; Mondal, B.; Xia, Z.; Chakraborty, S.; Nag, A. ns^2 Electron (Bi^{3+} and Sb^{3+}) doping in lead-free metal halide perovskite derivatives. *Chem. Mater.* **2020**, *32*, 10255−10267.

(14) Nabi, M.; Gupta, D. C. Potential lead-free small band gap halide double perovskites Cs_2CuMCl_6 (M = Sb, Bi) for green technology. *Sci. Rep.* **2021**, *11*, No. 12945.

(15) Bartel, C. J.; Clary, J. M.; Sutton, C.; Vigil-Fowler, D.; Goldsmith, B. R.; Holder, A. M.; Musgrave, C. B. Inorganic halide double perovskites with optoelectronic properties modulated by sublattice mixing. *J. Am. Chem. Soc.* **2020**, *142*, 5135−5145.

(16) Futscher, M. H.; Gangishetty, M. K.; Congreve, D. N.; Ehrler, B. Manganese doping stabilizes perovskite light-emitting diodes by reducing ion migration. *ACS Appl. Electron. Mater.* **2020**, *2*, 1522−1528.

(17) Lu, M.; Zhang, X.; Bai, X.; Wu, H.; Shen, X.; Zhang, Y.; Zhang, W.; Zheng, W.; Song, H.; Yu, W. W.; Rogach, A. L. Spontaneous silver doping and surface passivation of $CsPbI_3$ perovskite active layer enable light-emitting devices with an external quantum efficiency of 11.2%. *ACS Energy Lett.* **2018**, *3*, 1571−1577.

(18) Lin, K.; Xing, J.; Quan, L. N.; De Arquer, F. P. G.; Gong, X.; Lu, J.; Xie, L.; Zhao, W.; Zhang, D.; Yan, C.; et al. Perovskite light-emitting diodes with external quantum efficiency exceeding 20 per cent. *Nature* **2018**, *562*, 245−248.

(19) Yakunin, S.; Sytnyk, M.; Kriegner, D.; Shrestha, S.; Richter, M.; Matt, G. J.; Azimi, H.; Brabec, C. J.; Stangl, J.; Kovalenko, M. V.; Heiss, W. Detection of X-ray photons by solution-processed lead halide perovskites. *Nat. Photonics* **2015**, *9*, 444−449.

(20) Kim, J. Y.; Lee, J.-W.; Jung, H. S.; Shin, H.; Park, N.-G. High-efficiency perovskite solar cells. *Chem. Rev.* **2020**, *120*, 7867−7918.

(21) Chen, Q.; De Marco, N.; Yang, Y.; Song, T.-B.; Chen, C.-C.; Zhao, H.; Hong, Z.; Zhou, H.; Yang, Y. Under the spotlight: the organic−inorganic hybrid halide perovskite for optoelectronic applications. *Nano Today* **2015**, *10*, 355−396.

(22) Lee, J.-W.; Tan, S.; Seok Sang, I.; Yang, Y.; Park, N.-G. Rethinking the A cation in halide perovskites. *Science* **2022**, *375*, No. eabj1186.

(23) Bush, K. A.; Frohna, K.; Prasanna, R.; Beal, R. E.; Leijtens, T.; Swifter, S. A.; McGehee, M. D. Compositional engineering for efficient wide band gap perovskites with improved stability to photoinduced phase segregation. *ACS Energy Lett.* **2018**, *3*, 428−435.

(24) Chu, Z.; Zhao, Y.; Ma, F.; Zhang, C.-X.; Deng, H.; Gao, F.; Ye, Q.; Meng, J.; Yin, Z.; Zhang, X.; You, J. Large cation ethylammonium incorporated perovskite for efficient and spectra stable blue light-emitting diodes. *Nat. Commun.* **2020**, *11*, No. 4165.

(25) Stoumpos, C. C.; Cao, D. H.; Clark, D. J.; Young, J.; Rondinelli, J. M.; Jang, J. I.; Hupp, J. T.; Kanatzidis, M. G. Ruddlesden−popper

hybrid lead iodide perovskite 2D homologous semiconductors. *Chem. Mater.* **2016**, *28*, 2852−2867.
(26) Eperon, G. E.; Stone, K. H.; Mundt, L. E.; Schloemer, T. H.; Habisreutinger, S. N.; Dunfield, S. P.; Schelhas, L. T.; Berry, J. J.; Moore, D. T. The role of dimethylammonium in bandgap modulation for stable halide perovskites. *ACS Energy Lett.* **2020**, *5*, 1856−1864.
(27) Jiang, Y.; Cui, M.; Li, S.; Sun, C.; Huang, Y.; Wei, J.; Zhang, L.; Lv, M.; Qin, C.; Liu, Y.; Yuan, M. Reducing the impact of Auger recombination in quasi-2D perovskite light-emitting diodes. *Nat. Commun.* **2021**, *12*, No. 336.
(28) Mao, L.; Ke, W.; Pedesseau, L.; Wu, Y.; Katan, C.; Even, J.; Wasielewski, M. R.; Stoumpos, C. C.; Kanatzidis, M. G. Hybrid Dion−Jacobson 2D lead iodide perovskites. *J. Am. Chem. Soc.* **2018**, *140*, 3775−3783.
(29) Gao, P.; Bin Mohd Yusoff, A. R.; Nazeeruddin, M. K. Dimensionality engineering of hybrid halide perovskite light absorbers. *Nat. Commun.* **2018**, *9*, No. 5028.
(30) Xue, J.; Wang, R.; Chen, X.; Yao, C.; Jin, X.; Wang, K.-L.; Huang, W.; Huang, T.; Zhao, Y.; Zhai, Y.; Meng, D.; Tan, S.; Liu, R.; Wang, Z.-K.; Zhu, C.; Zhu, K.; Beard Matthew, C.; Yan, Y.; Yang, Y. Reconfiguring the band-edge states of photovoltaic perovskites by conjugated organic cations. *Science* **2021**, *371*, 636−640.
(31) Ju, M.-G.; Dai, J.; Ma, L.; Zhou, Y.; Zeng, X. C. Zero-dimensional organic−inorganic perovskite variant: Transition between molecular and solid crystal. *J. Am. Chem. Soc.* **2018**, *140*, 10456−10463.
(32) Morad, V.; Yakunin, S.; Benin, B. M.; Shynkarenko, Y.; Grotevent, M. J.; Shorubalko, I.; Boehme, S. C.; Kovalenko, M. V. Hybrid 0D antimony halides as air-stable luminophores for high-spatial-resolution remote thermography. *Adv. Mater.* **2021**, *33*, No. 2007355.
(33) Wei, J.-H.; Liao, J.-F.; Zhou, L.; Luo, J.-B.; Wang, X.-D.; Kuang, D.-B. Indium-antimony-halide single crystals for high-efficiency white-light emission and anti-counterfeiting. *Sci. Adv.* **2021**, *7*, No. eabg3989.
(34) Feng, S.; Ma, Y.; Wang, S.; Gao, S.; Huang, Q.; Zhen, H.; Yan, D.; Ling, Q.; Lin, Z. Light/force-sensitive 0D lead-free perovskites: from highly efficient blue afterglow to white phosphorescence with near-unity quantum efficiency. *Angew. Chem., Int. Ed.* **2022**, *61*, No. e202116511.
(35) Chen, H.; Zhu, L.; Xue, C.; Liu, P.; Du, X.; Wen, K.; Zhang, H.; Xu, L.; Xiang, C.; Lin, C.; Qin, M.; Zhang, J.; Jiang, T.; Yi, C.; Cheng, L.; Zhang, C.; Yang, P.; Niu, M.; Xu, W.; Lai, J.; Cao, Y.; Chang, J.; Tian, H.; Jin, Y.; Lu, X.; Jiang, L.; Wang, N.; Huang, W.; Wang, J. Efficient and bright warm-white electroluminescence from lead-free metal halides. *Nat. Commun.* **2021**, *12*, No. 1421.
(36) Ran, Q.; Zhang, Y.; Yang, J.; He, R.; Zhou, L.; Hu, S. White-light defect emission and enhanced photoluminescence efficiency in a 0D indium-based metal halide. *J. Mater. Chem. C* **2022**, *10*, 1999−2007.
(37) Han, P.; Luo, C.; Yang, S.; Yang, Y.; Deng, W.; Han, K. All-inorganic lead-free 0D perovskites by a doping strategy to achieve a plqy boost from <2% to 90%. *Angew. Chem., Int. Ed.* **2020**, *59*, 12709−12713.
(38) Zhou, L.; Liao, J.-F.; Huang, Z.-G.; Wei, J.-H.; Wang, X.-D.; Li, W.-G.; Chen, H.-Y.; Kuang, D.-B.; Su, C.-Y. A highly red-emissive lead-free indium-based perovskite single crystal for sensitive water detection. *Angew. Chem., Int. Ed.* **2019**, *58*, 5277−5281.
(39) Jing, Y.; Liu, Y.; Jiang, X.; Molokeev, M. S.; Lin, Z.; Xia, Z. Sb^{3+} Dopant and halogen substitution triggered highly efficient and tunable emission in lead-free metal halide single crystals. *Chem. Mater.* **2020**, *32*, 5327−5334.
(40) Kshirsagar, A. S.; Arfin, H.; Banerjee, S.; Mondal, B.; Nag, A. Colloidal Sb^{3+}-doped $Cs_2InCl_5{\cdot}H_2O$ perovskite nanocrystals with temperature-dependent luminescence. *J. Phys. Chem. C* **2021**, *125*, 27671−27677.
(41) Optical properties of low-Dimensional materials *WORLD SCIENTIFIC* 1996, p 436.
(42) Xu, L.-J.; Plaviak, A.; Lin, X.; Worku, M.; He, Q.; Chaaban, M.; Kim, B. J.; Ma, B. Metal halide regulated photophysical tuning of zero-dimensional organic metal halide hybrids: From efficient phosphorescence to ultralong afterglow. *Angew. Chem., Int. Ed.* **2020**, *59*, 23067−23071.
(43) Zhang, Z.; Saparov, B. Charge carrier mobility of halide perovskite single crystals for ionizing radiation detection. *Appl. Phys. Lett.* **2021**, *119*, No. 030502.
(44) Sun, S.; Lu, M.; Gao, X.; Shi, Z.; Bai, X.; Yu, W. W.; Zhang, Y. 0D Perovskites: Unique properties, synthesis, and their applications. *Adv. Sci.* **2021**, *8*, No. 2102689.
(45) Mohammed, O. F. Outstanding challenges of zero-dimensional perovskite materials. *J. Phys. Chem. Lett.* **2019**, *10*, 5886−5888.
(46) Lee, S.-H.; Jeong, S.; Seo, S.; Shin, H.; Ma, C.; Park, N.-G. Acid dissociation constant: A criterion for selecting passivation agents in perovskite solar cells. *ACS Energy Lett.* **2021**, *6*, 1612−1621.
(47) Gilli, P.; Pretto, L.; Bertolasi, V.; Gilli, G. Predicting hydrogen-bond strengths from acid−base molecular properties. the $_{p}$Ka slide rule: toward the solution of a long-lasting problem. *Acc. Chem. Res.* **2009**, *42*, 33−44.
(48) Sheikh, T.; Maqbool, S.; Mandal, P.; Nag, A. Introducing intermolecular cation-π interactions for water-stable low dimensional hybrid lead halide perovskites. *Angew. Chem., Int. Ed.* **2021**, *60*, 18265−18271.
(49) Bukvetskii, B. V.; Sedakova, T. V.; Mirochnik, A. G. Crystal structure and luminescence of antimony(III) chloride complex with anilinium chloride. *J. Struct. Chem.* **2009**, *50*, 149−152.
(50) Han, P.; Zhou, W.; Zheng, D.; Zhang, X.; Li, C.; Kong, Q.; Yang, S.; Lu, R.; Han, K. Lead-free all-inorganic indium chloride perovskite variant nanocrystals for efficient luminescence. *Adv. Opt. Mater.* **2022**, *10*, No. 2101344.
(51) McCall, K. M.; Morad, V.; Benin, B. M.; Kovalenko, M. V. Efficient lone-pair-driven luminescence: Structure−property relationships in emissive $5s^2$ metal halides. *ACS Mater. Lett.* **2020**, *2*, 1218−1232.
(52) Arfin, H.; Nag, A. Origin of luminescence in Sb^{3+}- and Bi^{3+}-doped Cs_2SnCl_6 perovskites: Excited state relaxation and spin−orbit coupling. *J. Phys. Chem. Lett.* **2021**, *12*, 10002−10008.
(53) Zhu, D.; Zaffalon, M. L.; Zito, J.; Cova, F.; Meinardi, F.; De Trizio, L.; Infante, I.; Brovelli, S.; Manna, L. Sb-Doped metal halide nanocrystals: A 0D versus 3D comparison. *ACS Energy Lett.* **2021**, *6*, 2283−2292.
(54) Berry, J.; Buonassisi, T.; Egger, D. A.; Hodes, G.; Kronik, L.; Loo, Y.-L.; Lubomirsky, I.; Marder, S. R.; Mastai, Y.; Miller, J. S.; Mitzi, D. B.; Paz, Y.; Rappe, A. M.; Riess, I.; Rybtchinski, B.; Stafsudd, O.; Stevanovic, V.; Toney, M. F.; Zitoun, D.; Kahn, A.; Ginley, D.; Cahen, D. Hybrid organic−inorganic perovskites (HOIPs): Opportunities and challenges. *Adv. Mater.* **2015**, *27*, 5102−5112.
(55) Egger, D. A.; Kronik, L. Role of dispersive interactions in determining structural properties of organic−inorganic halide perovskites: Insights from first-principles calculations. *J. Phys. Chem. Lett.* **2014**, *5*, 2728−2733.
(56) Munson, K. T.; Kennehan, E. R.; Doucette, G. S.; Asbury, J. B. Dynamic disorder dominates delocalization, transport, and recombination in halide perovskites. *Chem.* **2018**, *4*, 2826−2843.
(57) Momma, K.; Izumi, F. VESTA 3 for three-dimensional visualization of crystal, volumetric and morphology data. *J. Appl. Crystallogr.* **2011**, *44*, 1272−1276.
(58) Eickhoff, T.; Grosse, P.; Theiss, W. Diffuse reflectance spectroscopy of powders. *Vib. Spectrosc.* **1990**, *1*, 229−233.
(59) de Mello, J. C.; Wittmann, H. F.; Friend, R. H. An improved experimental determination of external photoluminescence quantum efficiency. *Adv. Mater.* **1997**, *9*, 230−232.
(60) Hohenberg, P.; Kohn, W. Inhomogeneous electron gas. *Phys. Rev.* **1964**, *136*, B864−B871.
(61) Kohn, W.; Sham, L. J. Self-consistent equations including exchange and correlation effects. *Phys. Rev.* **1965**, *140*, A1133−A1138.
(62) Blöchl, P. E. Projector augmented-wave method. *Phys. Rev. B* **1994**, *50*, 17953−17979.

(63) Kresse, G.; Joubert, D. From ultrasoft pseudopotentials to the projector augmented-wave method. *Phys. Rev. B* **1999**, *59*, 1758−1775.
(64) Kresse, G.; Furthmüller, J. Efficiency of ab-initio total energy calculations for metals and semiconductors using a plane-wave basis set. *Comput. Mater. Sci.* **1996**, *6*, 15−50.
(65) Perdew, J. P.; Ruzsinszky, A.; Csonka, G. I.; Vydrov, O. A.; Scuseria, G. E.; Constantin, L. A.; Zhou, X.; Burke, K. Restoring the density-gradient expansion for exchange in solids and surfaces. *Phys. Rev. Lett.* **2008**, *100*, No. 136406.
(66) Heyd, J.; Scuseria, G. E.; Ernzerhof, M. Hybrid functionals based on a screened Coulomb potential. *J. Chem. Phys.* **2003**, *118*, 8207−8215.
(67) Towns, J.; Cockerill, T.; Dahan, M.; Foster, I.; Gaither, K.; Grimshaw, A.; Hazlewood, V.; Lathrop, S.; Lifka, D.; Peterson, G. D.; Roskies, R.; Scott, J. R.; Wilkins-Diehr, N. XSEDE: Accelerating scientific discovery. *Comput. Sci. Eng.* **2014**, *16*, 62−74.

https://doi.org/10.1021/acs.chemmater.2c02737
Chem. Mater. 2022, 34, 10928−10939